

Central Lancashire Online Knowledge (CLoK)

Title	Spinning up a Daze: TESS Uncovers a Hot Jupiter orbiting the Rapid-Rotator TOI-778
Type	Article
URL	https://clock.uclan.ac.uk/45025/
DOI	https://doi.org/10.3847/1538-3881/acc3a0
Date	2023
Citation	Clark, Jake T., Addison, Brett C., Okumura, Jack, Vach, Sydney, Heitzmann, Alexis, Rodriguez, Joseph E., Wright, Duncan J., Clerte, Mathieu, Brown, Carolyn J. et al (2023) Spinning up a Daze: TESS Uncovers a Hot Jupiter orbiting the Rapid-Rotator TOI-778. <i>Astronomical Journal (AJ)</i> , 165 (5). ISSN 0004-6256
Creators	Clark, Jake T., Addison, Brett C., Okumura, Jack, Vach, Sydney, Heitzmann, Alexis, Rodriguez, Joseph E., Wright, Duncan J., Clerte, Mathieu, Brown, Carolyn J., Feterholf, Tara, Wittenmyer, Robert A., Plavchan, Peter, Kane, Stephen R., Horner, Jonathan, Kielkoff, John F., Shporer, Avi, Tinney, C. G., Hui-Gen, Liu, Ballard, Sarah, Bowler, Brendan P., Mengel, Matthew W., Zhou, George, Lee, Annette S., David, Avelyn, Heim, Jessica, Lee, Michele E., Sevilla, Veronica, Zafar, Naqsh E., Hinkel, Natalie R., Allen, Bridgette E., Bayliss, Daniel, Berberyan, Arthur, Berlind, Perry, Bieryla, Allyson, Bouchy, Francois, Brahm, Rafael, Bryant, Edward M., Christiansen, Jessie L., Ciardi, David R., Ciardi, Krys N., Collins, Karen A., Dallant, Jules, Davis, Allen B., Diaz, Matias R., Dressing, Courtney D., Esquerdo, Gilbert A., Harre, Jan-Vincent, Howell, Steve B., Jenkins, Jon M., Jensen, Eric L. N., Jones, Matias I., Jordan, Andres, Latham, David W., Lund, Michael B., McCormac, James, Nielsen, Louise D., Otegi, Jon, Quinn, Samuel N., Radford, Don J., Ricker, George R., Schwarz, Richard P., Seager, Sara, Smith, Alexis M. S., Stockdale, Chris, Tan, Thiam-Guan, Udry, Stephanie, Vanderspek, Roland, Gunther, Maximilian N., Wang, Songhu, Wingham, Geof and Winn, Joshua N.

It is advisable to refer to the publisher's version if you intend to cite from the work.
<https://doi.org/10.3847/1538-3881/acc3a0>

For information about Research at UCLan please go to <http://www.uclan.ac.uk/research/>

All outputs in CLoK are protected by Intellectual Property Rights law, including Copyright law. Copyright, IPR and Moral Rights for the works on this site are retained by the individual authors and/or other copyright owners. Terms and conditions for use of this material are defined in the <http://clock.uclan.ac.uk/policies/>



Spinning up a Daze: TESS Uncovers a Hot Jupiter Orbiting the Rapid Rotator TOI-778

Jake T. Clark¹ , Brett C. Addison^{1,2} , Jack Okumura¹ , Sydney Vach^{1,3} , Adriana Errico¹ , Alexis Heitzmann^{1,4} , Joseph E. Rodriguez⁵ , Duncan J. Wright¹ , Mathieu Clerté¹ , Carolyn J. Brown¹ , Tara Fetherolf^{6,51} , Robert A. Wittenmyer¹ , Peter Plavchan⁷ , Stephen R. Kane⁸ , Jonathan Horner¹ , John F. Kielkopf⁹ , Avi Shporer¹⁰ , C. G. Tinney¹¹ , Liu Hui-Gen¹² , Sarah Ballard¹³ , Brendan P. Bowler¹⁴ , Matthew W. Mengel¹ , George Zhou¹ , Annette S. Lee^{1,15,16,17} , Avelyn David^{15,16} , Jessica Heim^{15,16} , Michele E. Lee^{15,18} , Verónica Sevilla^{15,16} , Naqsh E. Zafar^{15,16} , Natalie R. Hinkel¹⁹ , Bridgette E. Allen^{20,21} , Daniel Bayliss²² , Arthur Berberyan^{20,23} , Perry Berlind³ , Allyson Bieryla³ , François Bouchy²⁴ , Rafael Brahm^{25,26,27} , Edward M. Bryant^{28,29} , Jessie L. Christiansen²⁰ , David R. Ciardi²⁰ , Krys N. Ciardi^{20,30} , Karen A. Collins³ , Jules Dallant²⁴ , Allen B. Davis^{31,32} , Matías R. Díaz^{33,34} , Courtney D. Dressing³⁵ , Gilbert A. Esquerdo³ , Jan-Vincent Harre³⁶ , Steve B. Howell³⁷ , Jon M. Jenkins³⁷ , Eric L. N. Jensen³⁸ , Matías I. Jones³⁹ , Andrés Jordán^{25,26,27} , David W. Latham³ , Michael B. Lund²⁰ , James McCormac⁴⁰ , Louise D. Nielsen²⁴ , Jon Otegi²⁴ , Samuel N. Quinn³ , Don J. Radford⁴¹ , George R. Ricker¹⁰ , Richard P. Schwarz³ , Sara Seager^{10,42,43} , Alexis M. S. Smith³⁶ , Chris Stockdale⁴⁴ , Thiam-Guan Tan^{45,46} , Stéphane Udry²⁴ , Roland Vanderspek¹⁰ , Maximilian N. Günther⁴⁷ , Songhu Wang⁴⁸ , Geof Wingham⁴⁹ , and Joshua N. Winn⁵⁰

¹ University of Southern Queensland, Centre for Astrophysics, USQ Toowoomba, West Street, QLD 4350 Australia; baddison2005@gmail.com

² Swinburne University of Technology, Centre for Astrophysics and Supercomputing, John Street, Hawthorn, VIC 3122, Australia

³ Center for Astrophysics | Harvard & Smithsonian, 60 Garden Street, Cambridge, MA 02138, USA

⁴ Astronomy Unit, Queen Mary University of London, Mile End Road, London E1 4NS, UK

⁵ Department of Physics and Astronomy, Michigan State University, East Lansing, MI 48824, USA

⁶ Department of Earth and Planetary Sciences, University of California Riverside, 900 University Avenue, Riverside, CA 92521, USA

⁷ Department of Physics & Astronomy, George Mason University, 4400 University Drive MS 3F3, Fairfax, VA 22030, USA

⁸ Department of Earth and Planetary Sciences, University of California, Riverside, CA 92521, USA

⁹ Department of Physics and Astronomy, University of Louisville, Louisville, KY 40292, USA

¹⁰ Department of Physics and Kavli Institute for Astrophysics and Space Research, Massachusetts Institute of Technology, Cambridge, MA 02139, USA

¹¹ Exoplanetary Science at UNSW, School of Physics, UNSW Sydney, NSW 2052, Australia

¹² School of Astronomy and Space Science, Key Laboratory of Modern Astronomy and Astrophysics in Ministry of Education, Nanjing University, Nanjing 210046, Jiangsu, People's Republic of China

¹³ Department of Astronomy, University of Florida, 211 Bryant Space Science Center, Gainesville, FL 32611, USA

¹⁴ Department of Astronomy, The University of Texas at Austin, TX 78712, USA

¹⁵ The Native Skywatchers Initiative, MN USA

¹⁶ Department of Physics and Astronomy, St. Cloud University, MN USA

¹⁷ Department of Astronomy and Astrophysics, University of California, Santa Cruz, CA 95064, USA

¹⁸ Jeremiah Horrocks Institute, University of Central Lancashire, Preston, PR1 2HE, UK

¹⁹ Space Science and Engineering Division, Southwest Research Institute, San Antonio, TX 78238, USA

²⁰ NASA Exoplanet Science Institute—Caltech/IPAC, 1200 E. California Blvd, Pasadena, CA 91125 USA

²¹ University of Wisconsin Stout, 712 South Broadway Street, Menomonie, WI 54751 USA

²² Dept. of Physics, University of Warwick, Gibbet Hill Road, Coventry, CV4 7AL, UK

²³ College of the Canyons, 26455 Rockwell Canyon Rd., Santa Clarita, CA 91355, USA

²⁴ Geneva Observatory, University of Geneva, Chemin Pegasi 51, 1290 Versoix, Switzerland

²⁵ Facultad de Ingeniería y Ciencias, Universidad Adolfo Ibáñez, Av. Diagonal las Torres 2640, Peñalolén, Santiago, Chile

²⁶ Millennium Institute for Astrophysics, Chile

²⁷ Data Observatory Foundation, Chile

²⁸ Dept. of Physics, University of Warwick, Gibbet Hill Road, Coventry CV4 7AL, UK

²⁹ Centre for Exoplanets and Habitability, University of Warwick, Gibbet Hill Road, Coventry CV4 7AL, UK

³⁰ Rhode Island College, 600 Mount Pleasant Avenue Providence, RI 02908 USA

³¹ Department of Astronomy, Yale University, 52 Hillhouse Avenue, New Haven, CT 06511, USA

³² International School of Boston, Cambridge, MA 02140, USA

³³ Las Campanas Observatory, Carnegie Institution of Washington, Colina el Pino, Casilla 601 La Serena, Chile

³⁴ Departamento de Astronomía, Universidad de Chile, Camino El Observatorio 1515, Las Condes, Santiago, Chile

³⁵ Astronomy Department, University of California, Berkeley, CA 94720, USA

³⁶ Institute of Planetary Research, German Aerospace Center (DLR), Rutherfordstraße 2, D-12489 Berlin, Germany

³⁷ NASA Ames Research Center, Moffett Field, CA 94035, USA

³⁸ Dept. of Physics & Astronomy, Swarthmore College, Swarthmore PA 19081, USA

³⁹ European Southern Observatory, Alonso de Córdova 3107, Vitacura, Casilla 19001, Santiago, Chile

⁴⁰ Dept. Physics, University of Warwick, Gibbet Hill Road, CV4 7AL, UK

⁴¹ Brierfield Observatory, New South Wales, Australia

⁴² Department of Earth, Atmospheric and Planetary Sciences, Massachusetts Institute of Technology, Cambridge, MA 02139, USA

⁴³ Department of Aeronautics and Astronautics, MIT, 77 Massachusetts Avenue, Cambridge, MA 02139, USA

⁴⁴ Hazelwood Observatory, Australia

⁴⁵ Perth Exoplanet Survey Telescope, Perth, Western Australia

⁴⁶ Curtin Institute of Radio Astronomy, Curtin University, Bentley, Western Australia 6102, Australia

⁴⁷ European Space Agency (ESA), European Space Research and Technology Centre (ESTEC), Keplerlaan 1, 2201 AZ Noordwijk, The Netherlands

⁴⁸ Department of Astronomy, Indiana University, Bloomington, IN 47405, USA

⁴⁹ Mt. Stuart Observatory, New Zealand

⁵⁰ Department of Astrophysical Sciences, Princeton University, Princeton, NJ 08544, USA

Received 2022 December 11; revised 2023 February 22; accepted 2023 March 8; published 2023 April 19

Abstract

NASA’s Transiting Exoplanet Survey Satellite (TESS) mission has been uncovering a growing number of exoplanets orbiting nearby, bright stars. Most exoplanets that have been discovered by TESS orbit narrow-line, slow-rotating stars, facilitating the confirmation and mass determination of these worlds. We present the discovery of a hot Jupiter orbiting a rapidly rotating ($v \sin i = 35.1 \pm 1.0 \text{ km s}^{-1}$) early F3V-dwarf, HD 115447 (TOI-778). The transit signal taken from Sectors 10 and 37 of TESS’s initial detection of the exoplanet is combined with follow-up ground-based photometry and velocity measurements taken from MINERVA-Australis, TRES, CORALIE, and CHIRON to confirm and characterize TOI-778 b. A joint analysis of the light curves and the radial velocity measurements yields a mass, a radius, and an orbital period for TOI-778 b of $2.76^{+0.24}_{-0.23} M_J$, $1.370 \pm 0.043 R_J$, and ~ 4.63 days, respectively. The planet orbits a bright ($V = 9.1$ mag) F3-dwarf with $M = 1.40 \pm 0.05 M_\odot$, $R = 1.70 \pm 0.05 R_\odot$, and $\log g = 4.05 \pm 0.17$. We observed a spectroscopic transit of TOI-778 b, which allowed us to derive a sky-projected spin-orbit angle of $18^\circ \pm 11^\circ$, consistent with an aligned planetary system. This discovery demonstrates the capability of smaller-aperture telescopes such as MINERVA-Australis to detect the radial velocity signals produced by planets orbiting broad-line, rapidly rotating stars.

Unified Astronomy Thesaurus concepts: Exoplanets (498); Radial velocity (1332); Transit photometry (1709); Dynamical evolution (421)

Supporting material: data behind figures, machine-readable table

1. Introduction

In the late 1980s, the first exoplanetary candidates around main-sequence stars were discovered orbiting Gamma Cephei (Campbell et al. 1988) and HD 114672 (Latham et al. 1989).⁵³ Soon after, Mayor & Queloz (1995) announced the discovery of 51 Peg b, the first planet found orbiting a Sun-like star—marking the start of the Exoplanet Era.

In the decade that followed that seminal discovery, the radial velocity technique dominated the search for exoplanets, revealing a plethora of “hot Jupiters”—giant planets orbiting their host stars with periods of just a few days (e.g., Butler et al. 1997; Henry et al. 2000; Tinney et al. 2001). Based solely on knowledge of the Solar System, it was broadly expected that planetary systems would feature giant planets on long-period orbits, and small, rocky worlds on short-period orbits.⁵⁴ Instead, it became obvious that a significant number of stars ($\sim 1\%$; see, e.g., Wittenmyer et al. 2011; Wright et al. 2012; Kunitomo & Matthews 2020) host scorching hot giant planets—marking their planetary systems as being truly exotic when compared to our own.

Such planets (commonly known as “hot Jupiters”) are by far the easiest exoplanets to detect—a fact made clear by the great success of the Kepler mission. Kepler launched in 2009 (see, e.g., Borucki et al. 2010), and spent slightly over four years staring continuously at a single patch of the night sky—in the northern constellation of Cygnus—monitoring the brightness of more than 150,000 stars. By recording minuscule dips in brightness exhibited by some of those stars, Kepler’s primary mission led to the discovery of 3251 planets. However, only a fraction (373, $\sim 11\%$) of those planets have both mass and radius measurements, as the majority of the

stars orbited by those planets are too faint for follow-up radial velocity mass measurements.⁵⁵

The successor to Kepler is the Transiting Exoplanet Survey Satellite, TESS (Ricker et al. 2015). Launched in 2018 April, TESS is currently in the process of scouring the sky, observing hundreds of thousands of the nearest and brightest stars, in an attempt to find short-period planets around them. TESS observes the majority of its targets for two consecutive 13.7 day periods, separated by a short window where the spacecraft pivots to broadcast data back to Earth. This means that it is particularly well adapted for the discovery of hot Jupiters, as transits of such planets are frequent (multiple transits are likely to occur during the ~ 27 day observing window) and deep. Indeed, the majority of the 291 planets⁵⁶ confirmed by TESS are either hot Jupiters or their smaller siblings, the “hot Neptunes” (e.g., Nielsen et al. 2019; Kossakowski et al. 2019; Plavchan et al. 2020; Jordán et al. 2020; Addison et al. 2021a, 2021b), and unlike the planets discovered by Kepler, a majority (271, $\sim 76\%$) of TESS planets have both mass and radius measurements.

The origins of hot Jupiters and Neptunes have been the source of much debate. It is widely accepted that such planets cannot have formed on their current orbits, so close to their host stars. Instead, it is thought that they originate at much greater distances, beyond the “ice line”—the location in the protoplanetary disk around their host at which temperatures were sufficiently low for water ice to be present (e.g., Pollack et al. 1996; Ida & Lin 2004; Wittenmyer et al. 2020).

Several different mechanisms have been proposed to explain this migration—all of which likely occur in some, but not all, planetary systems. The current proposals include a smooth process of migration through the protoplanetary disks of their host stars, as the young planet interacts with the material from which it is feeding (e.g., Lin et al. 1996; Tanaka et al. 2002); planet–planet scattering shifting the planet onto an extremely

⁵¹ UC Chancellor’s Fellow.

⁵³ This companion is likely a low-mass star in a face-on orbit (Kiefer 2019).

⁵⁴ For a detailed overview of our knowledge of the Solar System and its impact on our understanding of exoplanetary science, we direct the interested reader to Horner et al. (2020) and references therein.



Original content from this work may be used under the terms of the [Creative Commons Attribution 4.0 licence](https://creativecommons.org/licenses/by/4.0/). Any further distribution of this work must maintain attribution to the author(s) and the title of the work, journal citation and DOI.

⁵⁵ As of 2023 February 8th; statistics taken from the NASA Exoplanet Archive counts page, at https://exoplanetarchive.ipac.caltech.edu/docs/counts_detail.html.

⁵⁶ As of 2023 February 8th; data courtesy of the NASA Exoplanet Archive’s counts page.

eccentric orbit, followed by a process of tidal circularization (e.g., Chatterjee et al. 2008; Beaugé & Nesvorný 2012; Li et al. 2019a); and secular perturbations imposed by a highly inclined unseen massive companion (the Kozai–Lidov mechanism; Kozai 1962; Lidov 1962; Nagasawa et al. 2008; Nagasawa & Ida 2011).

For individual hot Jupiters, telltale signs of their formation pathways may still remain. The orbits of planets that migrate purely as a result of interaction with their host star’s protoplanetary disk are expected to remain coplanar with the star’s equator, as long as the initial disk is not tilted (as is the case for <100 Myr close-orbital giants AU Mic b, DS Tuc Ab, HIP 67522b, V1298 Tau b and c and TOI 942 c; see Plavchan et al. 2020; Zhou et al. 2020; Heitzmann et al. 2021; Gaidos et al. 2022), while a process of planet–planet scattering can act to moderately incline a planet’s orbit relative to that plane. Planets whose migration is driven by the Kozai–Lidov mechanism can become dramatically misaligned with the equators of their host stars—sometimes even being injected to polar or retrograde orbits (e.g., Albrecht et al. 2012; Addison et al. 2018; Siverd et al. 2018; Temple et al. 2019).

Studies of the inclination of the orbits of hot Jupiters have revealed a correlation between planetary inclination and host-star mass/temperature. The more massive (and hotter) the host star, the more likely it is that any short-period planets discovered in orbit will be strongly misaligned to the star’s equatorial plane (e.g., Collier Cameron et al. 2010; Addison et al. 2013; Rodríguez Martínez et al. 2020).

Given that more massive stars are more likely to exhibit binarity (Preibisch et al. 1999; Böhm-Vitense 2007), it is possible that the increased number of misaligned planets orbiting such stars is a direct result of those stars having undetected massive companions. Equally, more massive stars tend to form more massive planets (e.g., Ida & Lin 2005; Johnson et al. 2007; Bowler et al. 2010; Jones et al. 2016), and so mechanisms involving planet–planet scattering are also more likely to play a role in determining the obliquities of short-period planets.

To determine the degree to which these different mechanisms contribute to the overall population of short-period planets, it is important to discover and characterize as many such planets, orbiting as wide a variety of stars, as possible. In this work, we present the discovery of a new hot Jupiter orbiting HD 115447 (also known as TOI-778), an F3-dwarf with a mass of $1.39 \pm 0.02 M_{\odot}$ and a surface temperature of 6875 ± 190 K. The candidate planet was detected by TESS during Sector 10, in the first year of operation, as it surveyed the southern sky. Here, we used follow-up observations from a variety of ground-based facilities to confirm the existence of TOI-778 b and characterize both the planet and its orbit around TOI-778.

In Section 2, we describe the observations of TOI-778, followed in Section 3 by the latest characterization of the star from the observations we obtained. We then present the results of our analysis in Section 4, discuss those results in Section 5, and then conclude in Section 6.

2. Observations and Data Reduction

In this section, we describe the photometric, spectroscopic, and imaging data sets used to validate the planetary nature of TOI-778 b.

2.1. Photometric Observations

2.1.1. TESS Light Curve

TOI-778 (TIC 335630746) was observed by TESS during Sector 10 of its primary mission, from 2019 March 26 to April 21, and extended via Sector 37 observations, taken between 2021 April 2 and April 28. The target star was identified as a planet host candidate via the analyses of the Science Processing Observation Center (SPOC; Jenkins et al. 2016), as described by Jenkins (2002), Jenkins et al. (2010), Twicken et al. (2018), Li et al. (2019b), and Jenkins et al. (2020), using light curves extracted from the two-minute target pixel files. We used the Presearch Data Conditioning Simple Aperture Photometry flux values from the TESS light curve, removing nonzero flagged data (such as momentum dumps) that could contaminate the light-curve analysis. The light curves were then normalized by the median flux values and used in the analysis for TOI-778 b’s confirmation. The resulting light curves are found in Figure 1.

2.1.2. Next-Generation Transit Survey

A transit egress of TOI-778 b was observed using the Next-Generation Transit Survey (NGTS; Wheatley et al. 2018) on UTC 2019 June 22. NGTS is an exoplanet-hunting facility located at the ESO Paranal Observatory in Chile, which consists of 12 independently operated robotic telescopes. Each telescope has a 20 cm diameter and an 8 square-degree field-of-view. The NGTS telescopes use the DONUTS auto-guiding algorithm (McCormac et al. 2013) to achieve subpixel guiding. TOI-778 was observed simultaneously using two NGTS telescopes, and such multi-telescope observations have been shown to significantly improve the photometric precision of the observations (Bryant et al. 2020; Smith et al. 2020). A total of 1486 images were obtained using an exposure time of 10 s and the custom NGTS filter (520–890 nm). The airmass of the target was kept below 2 and the sky conditions were optimal throughout the observations.

The images were reduced using a custom aperture photometry pipeline (Bryant et al. 2020) that uses the SEP library (Bertin & Arnouts 1996; Barbary 2016) for source extraction and photometry. The pipeline automatically identifies comparison stars using Gaia DR2 (Gaia Collaboration et al. 2016, 2018), ranking the stars in the field based on their similarity to TOI-778 in terms of brightness, color, and CCD position.

2.1.3. Perth Exoplanet Survey Telescope

We observed an egress of TOI-778 on UTC 2020 March 31 in V band from the Perth Exoplanet Survey Telescope (PEST) near Perth, Australia. The 0.3 m telescope is equipped with a 1530×1020 SBIG ST-8XME camera with an image scale of $1''.2 \text{ pixel}^{-1}$, resulting in a $31' \times 21'$ field of view. A custom pipeline based on C-Munipack⁵⁷ was used to calibrate the images and extract the differential photometry, using an aperture with radius $7''.4$. The images have typical stellar point-spread functions (PSFs) with a full width at half maximum (FWHM) of $\sim 4''$.

2.1.4. LCO SAAO

We observed a full transit of TOI-778 in the Pan-STARSS z-short band on UTC 2020 May 30 from the LCOGT

⁵⁷ <http://c-munipack.sourceforge.net>

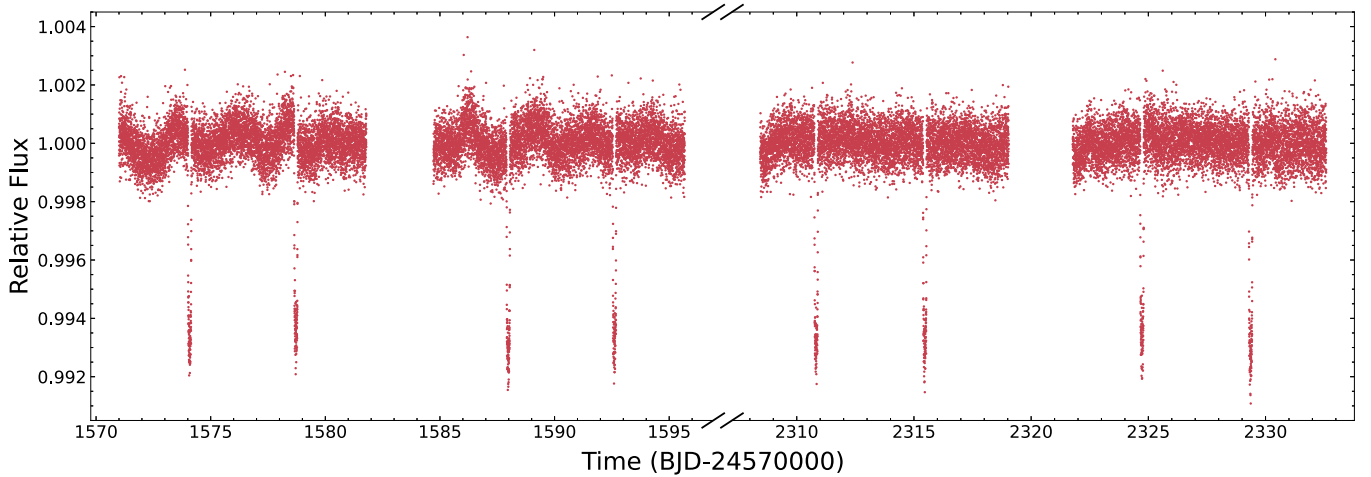


Figure 1. Full TESS PDCSAP median corrected light curves for TOI-778 from Sector 10 and Sector 37. The data behind this figure are available in machine-readable format.

(The data used to create this figure are available.)

(Brown et al. 2013) 1.0 m network node at South Africa Astronomical Observatory. We used the TESS Transit Finder, which is a customized version of the Tapir software package (Jensen 2013), to schedule our transit observations. The 4096×4096 LCOGT SINISTRO cameras have an image scale of $0''.389$ per pixel, resulting in a $26' \times 26'$ field of view. The images were calibrated by the standard LCOGT BANZAI pipeline (McCully et al. 2018), and photometric data were extracted with AstroImageJ (Collins et al. 2017). The images were defocused to an FWHM of $\sim 6''.7$, and circular apertures with radius $8''.2$ were used to extract the differential photometry.

2.1.5. Mount Kent Observatory

On 2020 June 5 at the Mount Kent Observatory, a photometric transit observation of TOI-778 was taken simultaneously with radial velocity observations from MINERVA-Australis. The observation was performed with the Shared Skies Partnership’s Planewave CDK700 telescope equipped with an Alta U16M Apogee camera. All data were taken using a Sloan i' filter with a $27''.3 \times 27''.3$ field of view. All data reduction and analysis was completed using the AstroImageJ software package.

2.1.6. Mt. Stuart

We observed TOI-778 b on UTC 2020 April 28 in the Sloan r' band from the Mt. Stuart Observatory near Dunedin, New Zealand. The 0.32 m telescope is equipped with a 3072×2048 SBIG STXL6303E camera with an image scale of $0''.88$ pixel $^{-1}$, resulting in a $44' \times 30'$ field of view. The images were calibrated and photometric data were extracted with AstroImageJ using a circular aperture with radius $3''.5$.

2.2. Spectroscopic Observations

In order to obtain precise radial velocity follow-up data and stellar properties for TOI-778, we carried out observations using four different facilities. Here, we give details about the observations carried out by each instrument.

2.2.1. MINERVA-Australis

We carried out the spectroscopic observations of TOI-778 using the MINERVA-Australis facility (Wittenmyer et al. 2018; Addison et al. 2019, 2021b). MINERVA-Australis consists of an array of four independently operated 0.7 m CDK700 telescopes situated at the Mount Kent Observatory in Queensland, Australia (Addison et al. 2019). Each telescope simultaneously feeds stellar light via fiber optic cables to a single KiwiSpec R4-100 high-resolution ($R = 80,000$) spectrograph (Barnes et al. 2012) with wavelength coverage from 480 to 620 nm. TOI-778 was observed on 71 epochs with three telescopes (labeled “T1, T3, T4”) between 2019 June 13 and 2020 June 4. Each epoch consists of two 30-minute exposures, and the resulting spectra had a signal-to-noise per resolution element (SNRe) range between 15 and 36. The resulting radial velocities and SNRe of each spectrum are given in Table 1. Radial velocities for the observations are derived for each telescope by cross-correlation, where the template being matched is the mean spectrum of each telescope. The instrumental variations are corrected by using simultaneous Thorium-Argon (ThAr) arc lamp observations. Radial velocities computed from different MINERVA-Australis telescopes are modeled in Section 4 as originating from independent instruments.

2.2.2. TRES

We obtained additional observations of TOI-778 via the Tillinghast Reflector Echelle Spectrograph (TRES; Fűrész 2008) on the 1.5 m reflector at the Fred Lawrence Whipple Observatory in Arizona, USA. TRES is a fiber-fed echelle with a resolving power of $R \sim 44,000$ over the wavelength range of 390–910 nm. Thirteen TRES radial velocities were collected between 2019 June 15 and 2020 February 29 using the standard observing procedure of obtaining a set of three science observations surrounded by ThAr calibration spectra. The science spectra are then combined to remove cosmic rays and wavelength calibrated using the ThAr spectra. The extraction technique follows procedures outlined in Buchhave et al. (2010). The spectra had an SNRe range between 41 and 79. The observation on the

Table 1
Radial Velocities for TOI-778

Time (BJD)	Velocity (m s ⁻¹)	Uncertainty (m s ⁻¹)	SNRe	Instrument
2458662.63164	227	129	46	Chiron
2458662.63531	-109	142	45	Chiron
2458662.63899	32	130	48	Chiron
2458664.59022	-70	103	61	Chiron
2458664.59389	166	110	59	Chiron
2458652.69011	-6229	133	7	Coralie
2458653.67374	-6090	131	19	Coralie
2458654.68544	-5971	106	5	Coralie
2458670.48753	-5466	56	53	Coralie
2458676.51154	-5935	66	48	Coralie
2458647.92621	-6528	149	24	M-A T1
2458647.94762	-7042	228	35	M-A T1
2458654.02680	-6794	189	29	M-A T1
2458665.04743	-6480	249	22	M-A T1
2458673.95523	-6876	96	30	M-A T1
2458647.92621	-6303	179	36	M-A T3
2458647.94762	-6453	200	19	M-A T3
2458654.02680	-6898	177	26	M-A T3
2458662.02455	-6579	229	27	M-A T3
2458662.04596	-6457	318	30	M-A T3
2459004.87332	-70	106	18	M-A T4RM
2459004.88826	73	82	24	M-A T4RM
2459004.90319	85	74	27	M-A T4RM
2459004.91813	198	84	23	M-A T4RM
2459004.93306	15	66	31	M-A T4RM
2458649.66043	182	100	57	TRES
2458651.66355	336	123	50	TRES
2458653.65718	-36	119	40	TRES
2458653.66621	-29	136	40	TRES
2458656.66766	615	126	54	TRES

Note. MINERVA-Australis is given as M-A.

(This table is available in its entirety in machine-readable form.)

night of 2020 July 29 was discarded due to a telescope issue combined with partly cloudy skies. We derived multi-order radial velocities using the remaining 12 spectra by cross correlating each spectrum, order-by-order, against the strongest SNRe spectrum.

2.2.3. CORALIE

The high-resolution spectrograph CORALIE (Queloz et al. 2001) is mounted on the Swiss 1.2 m Euler telescope at La Silla, Chile. The instrument is fed with a 2'' on-sky science fiber and a simultaneous Fabry-Pérot wavelength calibration fiber, with a resolution of $R = 60,000$. A total of 28 spectra of TOI-778 were obtained between 2019 June 17 and 2019 September 1 by the Swiss CORALIE team and the WINE-collaboration. One epoch was discarded due to low S/N, leaving 27 remaining spectra with SNRe 10–50 at a wavelength 550 nm. All spectra were extracted using the standard CORALIE data-reduction pipeline.

Radial velocities were extracted through the cross-correlation technique (Baranne et al. 1996). We used a weighted binary mask corresponding to an A0-star dominated by H and Fe lines. This mask highly favors the strongest 1000 absorption lines seen in hot stars (Wytttenbach et al. 2020). TOI-778 is a rapidly rotating star, resulting in non-Gaussian absorption lines. We therefore fit a rotational profile to the cross-correlation

functions, as done for WASP-189 in Anderson et al. (2018). Through this method, we achieve a typical radial velocity precision of 80 m s^{-1} .

2.2.4. CHIRON

We obtained 27 spectra of TOI-778 using the CHIRON spectrograph (Tokovinin et al. 2013) on the Small and Moderate Aperture Research Telescope System (SMARTS) 1.5 m telescope at Cerro Tololo, Chile. The CHIRON spectra were obtained using the $R = 80,000$ slicer mode, and each spectrum is bracketed by a pair of ThAr lamp exposures for wavelength calibration.

This combination allows for higher throughput at the cost of some instrumental radial velocity precision. For this early-type star, however, the radial velocity uncertainties are dominated by the broad and sparse spectral lines, rather than wavelength calibration errors or line-spread function drifts (both of which are better addressed with the iodine cell, rather than ThAr). CHIRON's fiber has an on-sky radius of $1''.35$ with individual exposure times set to 5 minutes in length. Three back-to-back exposures were taken per night that we observed TOI-778.

The radial velocities were derived following the procedure described in Jones et al. (2017), Wang et al. (2019), and Davis et al. (2020). To summarize, each set of observations of TOI-778 during a night was followed by a ThAr exposure, and the CHIRON pipeline (Paredes et al. 2021) uses this lamp to compute a new wavelength solution; this method yields a demonstrated long-term stability of $\sim 15 \text{ m s}^{-1}$, on bright targets. Individual CHIRON spectra are shifted to a common rest frame and then stacked to form a template. We compute the Cross-Correlation Function (CCF) between each observed spectrum and this template. We then fit a Gaussian function plus linear trend to the CCF, and take the maximum of the fit to be the radial velocity for that observation. This method is repeated for the 33 echelle orders between ~ 470 and 650 nm where we have good wavelength calibration. The final radial velocity at each epoch is obtained from the median of the individual order velocities, after applying a 3σ rejection method. Radial velocity uncertainties are computed from the error in the mean of the nonrejected velocities (as in Jones et al. 2017). For this star, the typical radial velocity error found was about 150 m s^{-1} .

2.3. High Angular Resolution Imaging

As part of our standard process for validating transiting exoplanets to assess the possible contamination of bound or unbound companions on the derived planetary radii (Ciardi et al. 2015), we observed TOI-778 with high-resolution near-infrared adaptive optics (AO) imaging at Palomar and Keck Observatories and with optical speckle interferometric imaging at Gemini-South. The infrared observations provide the deepest sensitivities to faint companions, while the optical speckle observations provide the highest-resolution imaging, making the two techniques complementary. Additionally, because the speckle interferometry overlaps with the TESS band pass, no assumptions needed to be made about the SED of possible contaminants.

2.3.1. Near-infrared AO

The Palomar Observatory observations were made with the Palomar High Angular Resolution Observer (PHARO)

instrument (Hayward et al. 2001) behind the natural guide star AO system P3K (Dekany et al. 2013) on 2020 Jun 12 UT in a standard five-point quincunx dither pattern with steps of $5''$ in the narrowband $Br - \gamma$ filter ($\lambda_o = 2.1686$; $\Delta\lambda = 0.0326 \mu\text{m}$). Each dither position was observed three times, offset in position from each other by $0''.5$ for a total of 15 frames; with an integration time of 10 s per frame, the total on-source time was 150 s. PHARO has a pixel scale of $0''.025$ per pixel for a total field of view of $\sim 25''$.

The Keck Observatory observations were made with the NIRC2 instrument on Keck II behind the natural guide star AO system (Wizinowich et al. 2000) on 2019 June 25 in the standard three-point dither pattern that is used with NIRC2 to avoid the left lower quadrant of the detector, which is typically noisier than the other three quadrants. The dither pattern step size was $3''$ and was repeated twice, with each dither offset from the previous dither by $0''.5$. NIRC2 was used in the narrow-angle mode with a full field of view of $\sim 10''$ and a pixel scale of approximately 10 milliarcsec per pixel. The Keck observations were made in both the narrowband $Br - \gamma$ ($\lambda_o = 2.1686$; $\Delta\lambda = 0.0326 \mu\text{m}$) and the $J - \text{cont}$ ($\lambda_o = 1.2132$; $\Delta\lambda = 0.0198 \mu\text{m}$) filters with an integration time for each filter of 1 s, for a total of 9 s on target.

The AO data were processed and analyzed with a custom set of IDL tools. The science frames were flat-fielded and sky-subtracted. The flat fields were generated from a median average of dark subtracted flats taken on-sky. The flats were normalized such that the median value of the flats is unity. The sky frames were generated from the median average of the 15 dithered science frames; each science image was then sky-subtracted and flat-fielded. The reduced science frames were combined into a single combined image using an intrapixel interpolation that conserves flux, shifts the individual dithered frames by the appropriate fractional pixels, and median-coadds the frames. The final resolution of the combined dithers was determined from the full width at half maximum of the point-spread function: $0''.105$ and $0''.050$ for the Palomar and Keck observations, respectively.

To within the limits of the AO observations, no stellar companions were detected. The sensitivities of the final combined AO image were determined by injecting simulated sources azimuthally around the primary target every 20° at separations of integer multiples of the central source's FWHM (Furlan et al. 2017). The brightness of each injected source was scaled until standard aperture photometry detected it with 5σ significance. The resulting brightness of the injected sources relative to TOI-778 set the contrast limits at that injection location. The final 5σ limit at each separation was determined from the average of all of the determined limits at that separation, and the uncertainty on the limit was set by the rms dispersion of the azimuthal slices at a given radial distance (Figure 2).

2.4. Optical Speckle Interferometry

TOI-778 was observed on 2020 March 16, using the Zorro speckle interferometric instrument mounted on the 8 m Gemini South telescope on the summit of Cerro Pachon in Chile. Zorro simultaneously obtains diffraction-limited images at 562 and 832 nm. Our data set consisted of 3 minutes of total integration time on source, taken as sets of 1000×0.06 s images, plus a consecutive observation of a PSF standard star. Following Howell et al. (2011), we combined all images and subjected

them to Fourier analysis to produce speckle reconstructed imagery from which the 5σ contrast curves are derived for each passband and nearby companion stars are searched for (Figure 3). Our data reveal TOI-778 to be a single star to contrast limits of 5–8.5 mag, covering a spatial range of ~ 3 –196 au at the distance to TOI-778.

3. Stellar Properties of HD 115447

The planetary properties of TOI-778 b depend upon the stellar properties of its host star. We first combine the MINERVA-Australis spectra of TOI-778 to create a median spectrum to input into *iSpec* (Blanco-Cuaresma et al. 2014; Blanco-Cuaresma 2019). *iSpec* uses a grid-modeling approach to calculate the effective temperature (T_{eff}), surface gravity ($\log g$) and overall metallicity ($[M/H]$) from the input spectra. These spectroscopic properties are then used along with other photometric and astrometric data as input for the Bayesian isochrone modeling program *isochrones*. We used the Gaia DR2 (Gaia Collaboration et al. 2018) parallax and magnitudes (G , G_R , and G_B), 2MASS (Cutri et al. 2003) magnitudes (J , H , and K_s), V-band magnitude (V), and color excess ($E(B-V)$), with the *iSpec* values as input for the *isochrones* analysis. The resulting derived isochrone properties for TOI-778, including stellar mass, radius, luminosity, and age, are given in Table 2. Our results are consistent with version 9 of the TESS Input Catalog (Stassun et al. 2019) and are the parameters used to further characterize the planetary nature of TOI-778 b. The above procedure of determining the stellar properties of TOI-778 is similar to that of Addison et al. (2021b).

We also calculated the rotation period of TOI-778 through the light curve obtained by TESS (discussed in more detail within Section 2.1). Using SCIPY's Lomb–Scargle periodogram (Virtanen et al. 2020) on the light curves collected by TESS (plotted in Figure 1), we performed the analysis in two search ranges: 0.01–1.5 days and 1–13 days. The periodogram analysis was part of a larger Variability Catalog of TESS light curves (see Fetherolf et al. 2022), and TOI-778 did make it into the final Variability Catalog after several careful vetting steps to remove false positives that could be caused by spacecraft systematics (e.g., momentum dumps).

A significant signal was found in the 1–13 day periodogram search, corresponding to a stellar rotation period for TOI-778 to be 2.567 ± 0.095 days. Figure 4 shows a phase-folded plot of TOI-778's light curve to the period of 2.567 days. There seems to be no correlation between the light-curve modulation and the momentum dumps of TESS shown in Figure 4, and the normalized power of the periodogram is sufficiently high that we are confident this modulation is astrophysical in nature. We include our derived stellar rotation value in Table 2.

4. Joint Analysis and Results

To determine the planetary nature of TOI-778 b, as well as its host star's obliquity, we used *Allesfitter* (Günther & Daylan 2019, 2021) to perform a joint analysis of the TESS light-curve segments, the photometric ground-based light curves, and the radial velocity measurements. We include both light curves from the TESS Sectors 10 and 37, keeping them as separate observations with possible brightness offsets between the sectors. We also split the observations from each sector into two parts, because there is a clear break in each sector during

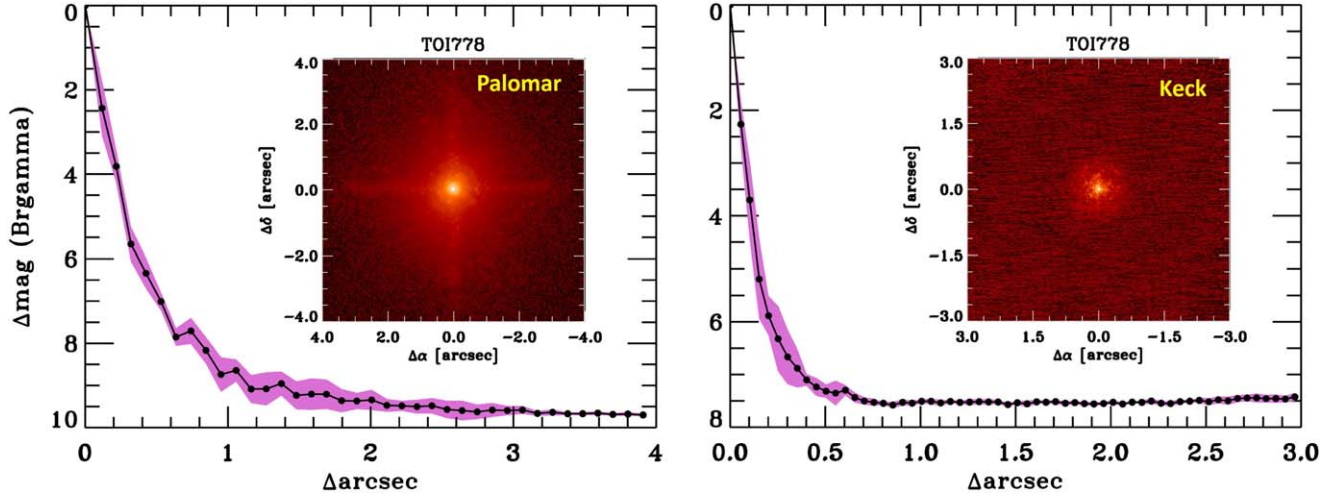


Figure 2. Companion sensitivity for the near-infrared adaptive optics imaging. The black points represent the 5σ limits and are separated in steps of 1 FWHM; the purple represents the azimuthal dispersion (1σ) of the contrast determinations (see Section 2.3). The inset image is of the primary target, showing no additional close-in companions.

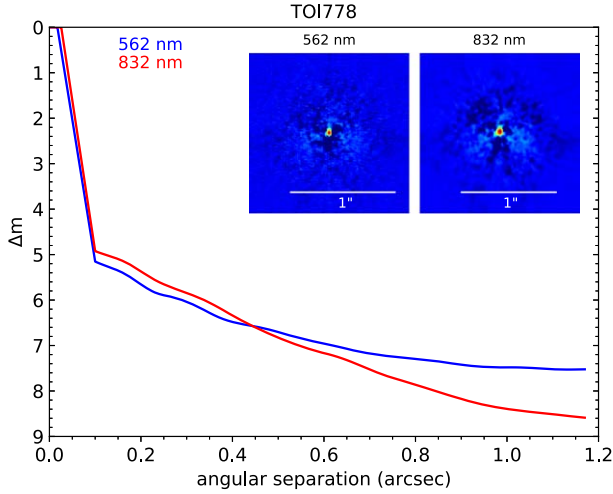


Figure 3. Speckle interferometric contrast curves and reconstructed images for the 562 and 832 nm observations. No companion was detected within the spatial limits of the diffraction limit and $1.2''$ equaling 3–4 to 196 au at the distance of TOI-778.

the data download. Thus, we have four independent TESS light curves we use for the analysis. We use all ground-based photometric observations of TOI-778 that include at least 50% of the transits of TOI-778 b. These facilities included the NGTS, PEST, LCO, Mt. Kent, and Mt. Stuart observations. We used all radial velocity measurements taken from MINERVA-Australis, TRES, CORALIE, and CHIRON. These radial velocities include the data from MINERVA-Australis that were taken during the Rossiter–McLaughlin observation on 2020 June 4. TOI-778’s stellar radius, mass, and effective temperature are used within the *Allesfitter* analysis, as these values are needed for deriving the planetary mass, radius, and equilibrium temperature.

The priors used for our analysis are given in Tables 2, 3, and 4, and described below. For each of our light curves, we calculated the quadratic limb-darkening coefficients used by Eastman et al. (2013), an interpolation of the quadratic limb-darkening tables derived by Claret & Bloemen (2011). These calculated values were then used as the starting values for the

limb-darkening coefficient parameters with uniform priors between 0 and 1 within the *Allesfitter* analysis. Because NGTS has a unique band-pass filter, we set its initial quadratic limb-darkening coefficients to 0.5 with a uniform prior between 0 and 1. We fixed the dilution parameter to 0 because the TESS SPOC light curves used in the analysis already have any potential blending removed from the target star’s flux from known sources. For the physical parameters used in the *Allesfitter* analysis, we applied uniform priors with starting values taken from or derived from NASA’s Exoplanet Follow-up Observing Program database for the orbital period (P_p), transit mid-time ($T_{0,b}$), planet-to-star radius ratio (R_p/R_*), the ratio of the sum of the planet and star radii to the semimajor axis ($(R_p + R_*)/a_p$), cosine of the inclination angle ($\cos i_p$), the radial velocity semi-amplitude (K), and eccentricity ($\sqrt{e_p} \cos \omega_p$ and $\sqrt{e_p} \sin \omega_p$). Uniform priors were used for the light curves’ flux error scaling ($\ln \sigma_{F_{\text{inst}}}$) as well as on the radial velocity baseline offsets (ΔRV_{inst}) and jitter terms ($\ln \sigma_{RV_{\text{inst}}}$) for each instrument. Included in the joint fit was the Rossiter–McLaughlin effect, and for this we applied a weak (5σ) Gaussian prior on the stellar rotational velocity ($v \sin(i)$) as derived using spectroscopic observations from TRES (see Table 2).

We utilize *Allesfitter*’s nested sampling approach to sample the model posteriors by implementing the *dynesty* package (Speagle 2020). We used a dynamic nested sampling, with random walk sample, 500 live points, and a tolerance of 0.01. We ran our analysis until a tolerance of 0.01 was achieved with the derived stellar, planetary, and instrumental parameters shown in Tables 3 and 4 (in the Appendix). Median values are shown in Tables 3 and 4 along with their associated 1σ errors.

The resulting transit light-curve model for the TESS and ground-based photometry can be found in Figures 5 and 6, respectively. Figure 5 also includes the radial velocity model for TOI-778 b with our Doppler spectroscopy data. From the global analysis, TOI-778 b’s orbital period is 4.633611 ± 0.000001 days, in line with the 4.63361 ± 0.00011 days found by TESS in Sector 10. It has a relatively large radial velocity semi-amplitude, with a 16σ detection of $K = 271^{+18}_{-17} \text{ m s}^{-1}$. Given these parameter posteriors, along with our estimates of the stellar mass, radius, and

Table 2
Stellar Parameters for HD 115447

Stellar Parameters	Value	Source
Catalog Information		
R.A. (h:m:s)	13:17:20.189	1
decl. (d:am:as)	−15:16:24.944	1
Parallax (mas)	6.15415 ± 0.04231	1
$\mu_{R.A.}$ (mas yr ^{−1})	$−60.600 \pm 0.083$	1
$\mu_{decl.}$ (mas yr ^{−1})	$−26.012 \pm 0.065$	1
Gaia DR2 ID	3607877948613218304	1
2MASS ID	J13172019-1516248	2
HD ID	115447	
TIC ID	335630746	3
TOI ID	778	
Spectroscopic Properties		
Spectral type	F2	4
	F3V	5
T_{eff} (K)	6715 ± 128	3
	6875 ± 190 [†]	7
	6643 ± 150 ^{‡,*}	7
$\log g$ (cgs)	4.144 ± 0.085	3
	4.05 ± 0.17 [†]	7
	3.98 ± 0.22 [‡]	7
Metallicity, [m/H]	0.00 ± 0.08 [†]	7
Metallicity, [m/H]	0.03 ± 0.08 [‡]	7
$v \sin i$ (km s ^{−1})	28.9 ± 3.7 [†]	7
	35.1 ± 1.0 ^{‡,*,\wedge}	7
Photometric Properties		
G (mag)	8.9944 ± 0.0007	1
G_{BP} (mag)	9.226 ± 0.002	1
G_{RP} (mag)	8.648 ± 0.002	1
J (mag)	8.25 ± 0.02	2
H (mag)	8.09 ± 0.03	2
K_s (mag)	8.055 ± 0.033	2
V (mag)	9.11 ± 0.02	6
T (mag)	8.690 ± 0.006	3
Derived Stellar Properties		
M_* (M_{\odot})	1.428 ± 0.094	3
	1.40 ± 0.05 [*]	7
R_* (R_{\odot})	1.677 ± 0.068	3
	1.71 ± 0.05 [*]	7
ρ_* (g cm ^{−3})	0.40 ± 0.03	7
L_* (L_{\odot})	5.153 ± 0.269	3
	5.76 ± 0.65	7
Age (Gyr)	$1.95^{+0.14}_{-0.13}$	7
Distance (pc)	162 ± 1	1
Rotation Period (days)	2.584 ± 0.095	7

Note. [†]Derived using MINERVA-Australis spectroscopic observations. [‡]Derived using spectroscopic observations from TRES. ^{*}Preferred solution and used as a prior in the *Allesfitter* analysis. ^{\wedge}Lower limit placed on $v \sin i$ uncertainty of ± 1.0 km s^{−1}, due to contributions of other sources of absorption line-broadening.

References. (1) Gaia Collaboration et al. 2018; (2) Cutri et al. 2003; (3) Stassun et al. 2019; (4) Cannon & Pickering 1993; (5) Houk & Smith-Moore 1988; (6) Høg et al. 2000; (7) This work.

their uncertainties given in Table 2, we derive the planetary mass, radius, and bulk density for TOI-778 b to be $2.8 \pm 0.2 M_J$, $1.37 \pm 0.04 R_J$, and $\rho_p = 1.3 \pm 0.2$ cgs, respectively. With its radius and orbital period, we confirm the planetary nature of TOI-778 b as a hot Jupiter.

TOI-778 b was found to have a statistically significant, nonzero orbital eccentricity of 0.21 ± 0.04 . With previous research showing that eccentric orbits can exist due to hidden planetary companions (e.g., Wittenmyer et al. 2013;

Trifonov et al. 2017; Boisvert et al. 2018; Wittenmyer et al. 2019), we further inspected the radial velocity residuals using a general Lomb–Scargle periodogram, but found no significant signals. We also performed an independent analysis of our radial velocity and photometric data through EXOFASTv2 (Eastman 2017; Eastman et al. 2019) and found consistent results at the 1σ level.

We also conducted a joint analysis of the Rossiter–McLaughlin observation (Minerva T4RM) with the global fit to measure the sky-projected spin–orbit alignment of the system. The resulting effect can clearly be seen in Figures 5 and 7. The global fit analysis yields a sky-projected spin–orbit angle of $18^\circ \pm 11^\circ$. In addition, following Masuda & Winn (2020), we find the stellar inclination to be well-aligned to the line of sight, with $I_* > 50^\circ$ at 3σ significance. This result is consistent with an aligned system and is discussed further in Section 5.

5. TOI-778 b in Context

We have confirmed the planetary nature of TOI-778 b, detected by TESS in Sector 10 of its primary mission. It is a hot Jupiter with radius $1.37 \pm 0.04 R_J$ and mass $2.8 \pm 0.2 M_J$, orbiting a rapidly rotating early-F star. TOI-778 b appears to be somewhat inflated when compared to other hot Jupiters of similar masses.

The confirmation and mass measurement of TOI-778 b were challenging due to the relatively rapid ~ 35 km s^{−1} rotation of its early-F type host star. Figure 8 shows the stellar rotational velocity against the semi-amplitude radial velocity precision of all known exoplanets with a mass measurement precision better than 20%.

There are only five other planets that have been discovered with a mass precision of better than 20%, orbiting around more rapidly rotating stars. These include CoRoT-11 b (Gandolfi et al. 2010), HAT-P-69 b (Zhou et al. 2019b), HATS-70 b (Zhou et al. 2019a), Kepler-1658 b (Chontos et al. 2019), and WASP-93 b (Hay et al. 2016). In the most extreme case, HAT-P-69 b was found around a rapidly rotating A-type star ($v \sin i = 77.44 \pm 0.56$ km s^{−1}), and achieved a semi-amplitude radial velocity precision of $K = 309 \pm 49$ m s^{−1}. Our results demonstrates how a facility like MINERVA-Australis, with an effective telescope radius of 1.20 m, can be utilized to follow up and confirm planetary candidates around such rapidly rotating stars.

Hot Jupiters appear to be less frequent around early-type stars than solar-like stars (Sebastian et al. 2022; Beleznyay & Kunitomo 2022), with Zhou et al. (2019c) discovering an occurrence rate in TESS data of only $0.43\% \pm 0.15\%$ for hot Jupiters orbiting main-sequence F-type stars and $0.26\% \pm 0.11\%$ for A-type stars. These low occurrence rates for earlier-type stars are consistent with those found for their evolved kin (Grunblatt et al. 2019).

The rapid rotation, brightness ($V = 9.1$ mag), and large radius of the planet all work in favor of measuring the spin–orbit angle for this system. From Rossiter–McLaughlin observations of a transit of TOI-778 b, we find the planet’s orbit to be close to being aligned with the stellar equator, with a host-star sky-projected obliquity of $19^\circ \pm 10^\circ$.

An obliquity measurement can aid in better determining the origin and formation history of exoplanets, especially large and relatively close-in orbiting ones like TOI-778 b. Because the star’s effective temperature ($T_{\text{eff}} \sim 6700$ K) is beyond the Kraft

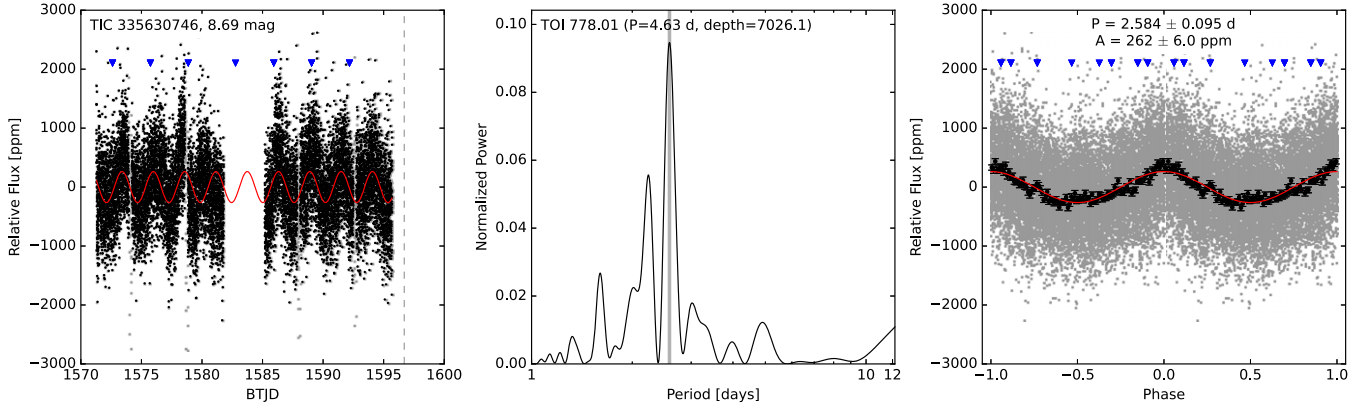


Figure 4. Left: Relative flux values from TOI-778 during Sector 10 (black dots). The transit events of TOI-778 b that have been removed for the periodogram analysis are shown as gray points, with the periodic signal of 2.584 days overplotted in red. Momentum dumps from TESS are shown by the blue triangles. Center: The periodogram from the TESS light curve. The transits have been removed from the light curve for the periodogram analysis, such that the periodogram appears to be near zero at 4.5 days. Right: A phase-folded version of the leftmost figure, with the period and semi-amplitude of the periodic variations listed at the top of the figure.

Table 3
Astrophysical Parameters for TOI-778 b as Derived by *Allesfitter*

Parameter	Prior	Best Fit
Fitted Planetary Parameters		
K_b (m s ⁻¹)	$\mathcal{U}(10,1000)$	271 ± 17
R_p/R_*	$\mathcal{U}(0.01,0.2)$	0.0825 ± 0.0005
$(R_* + R_p)/a_p$	$\mathcal{U}(0.05,0.2)$	0.143 ± 0.004
$\cos i$	$\mathcal{U}(0,0.2)$	$0.091^{+0.006}_{-0.005}$
$T_{0,b} - 2458000$ (BJD)	$\mathcal{U}(577.7, 579.7)$	578.7161 ± 0.0001
P_b (d)	$\mathcal{U}(3.6, 5.6)$	4.633611 ± 0.000001
$\sqrt{e_b} \cos \omega_b$	$\mathcal{U}(-0.9, 0.9)$	$0.40^{+0.06}_{-0.07}$
$\sqrt{e_b} \sin \omega_b$	$\mathcal{U}(-0.9, 0.9)$	0.21 ± 0.07
Derived Planetary Parameters		
a_p/R_*		7.6 ± 0.2
R_p (R_\oplus)		15.4 ± 0.5
M_p (M_\oplus)		878^{+77}_{-72}
i_p (deg)		$84.7^{+0.3}_{-0.4}$
e_p		0.21 ± 0.04
w_p (deg)		28^{+12}_{-10}
R_p (R_{jup})		1.37 ± 0.04
M_p (M_{jup})		2.8 ± 0.2
a_p (AU)		0.060 ± 0.003
b_{trap}		0.61 ± 0.02
$T_{\text{tot},p}$ (hr)		3.76 ± 0.01
$T_{\text{full},p}$ (hr)		2.89 ± 0.01
ρ_p (cgs)		1.3 ± 0.2
$T_{\text{eq},p}$ (K)		1561^{+33}_{-32}
Stellar Parameters		
$v \sin i$ (km s ⁻¹)	$\mathcal{N}(35.1, 5.0)$	$39.9^{+4.5}_{-4.3}$
λ (deg)	$\mathcal{U}(-180, 180)$	18 ± 11
ρ_* (cgs, derived)		0.38 ± 0.03

Notes. Priors are shown as uniform $\mathcal{U}(a,b)$ or normal $\mathcal{N}(\mu,\sigma)$. Parameters used for the transit and radial velocity fits that are not located in this table can be found in Table 4.

break temperature of ~ 6200 K, it is unlikely to have realigned from a high-obliquity orbit (Kraft 1967). Thus, we may be seeing the exoplanet’s primordial obliquity, rather than the result of a secondary realignment. It therefore seems most likely that TOI-778 b sedately migrated through its host’s disk, rather than reaching its current location through more chaotic means. Indeed, with a low obliquity angle and a stellar age of

~ 2 Gyr, migration mechanisms such as high-eccentricity, planet–planet scattering, Kozai–Lidov tidal, and secular chaos migrations are disfavored (Masset & Papaloizou 2003; Nagasawa et al. 2008; Dawson & Johnson 2018).

While the radial velocity data are limited and noisy, we can also exclude the presence of perturbing objects more massive than $\sim 6 M_J$ within 0.3 au. Additionally, based on the estimated sensitivity of the high angular resolution imaging from Gemini, Keck, and Palomar (Section 2.3), along with the Pecaute & Mamajek (2013) table of stellar properties, we can place upper mass limits for potential stellar companions in this system as $0.73 M_\odot$ at a distance of 9.2 au (separation of $0''.057$, equivalent to 1 FWHM from the star for Keck NIRC2), $0.16 M_\odot$ at 40.4 au ($0''.25$), and $0.10 M_\odot$ at 80.9 au ($0''.50$). Combined, the radial velocity and direct imaging data cannot fully rule out massive planetary, substellar, or low-mass stellar objects with masses $< 0.16 M_\odot$ within ~ 40 au; therefore, planet–planet scattering and Kozai–Lidov tidal migration remain potentially viable migration mechanisms for TOI-778 b.

Figure 9 shows the planetary obliquity as a function of host-star temperature with TOI-778 b and the sample of known hot Jupiters with obliquity measurements. From Figure 9, TOI-778 b joins a cohort of other hot Jupiters with well-aligned orbits, suggesting that disk migration is the likely cause of their evolution to their current positions.

6. Conclusion

During Sector 10 of TESS’s primary mission, an exoplanet candidate was discovered around the rapidly rotating star HD 115447, also known as TOI-778. This 4.63 day signal was subsequently followed up by the exoplanetary community through transit observations from PEST, LCO, NGTS, Mount Kent, and Mt. Stuart. Coinciding with these efforts, radial velocity measurements from TOI-778 were collected from MINERVA-Australis, TRES, CORALIE, and CHIRON, to then determine the exoplanetary nature of TOI-778 b. From our *AllesFitter* global model, we confirm the presence of the hot Jupiter TOI 778 b ($1.37 \pm 0.04 R_J$, $2.8 \pm 0.2 M_J$). We conducted a Rossiter–McLaughlin observation of TOI-778 b and discovered that its spin–orbit angle to its host is $18^\circ \pm 11^\circ$, which is consistent with an aligned planetary system. These results also highlight how smaller telescope arrays such as

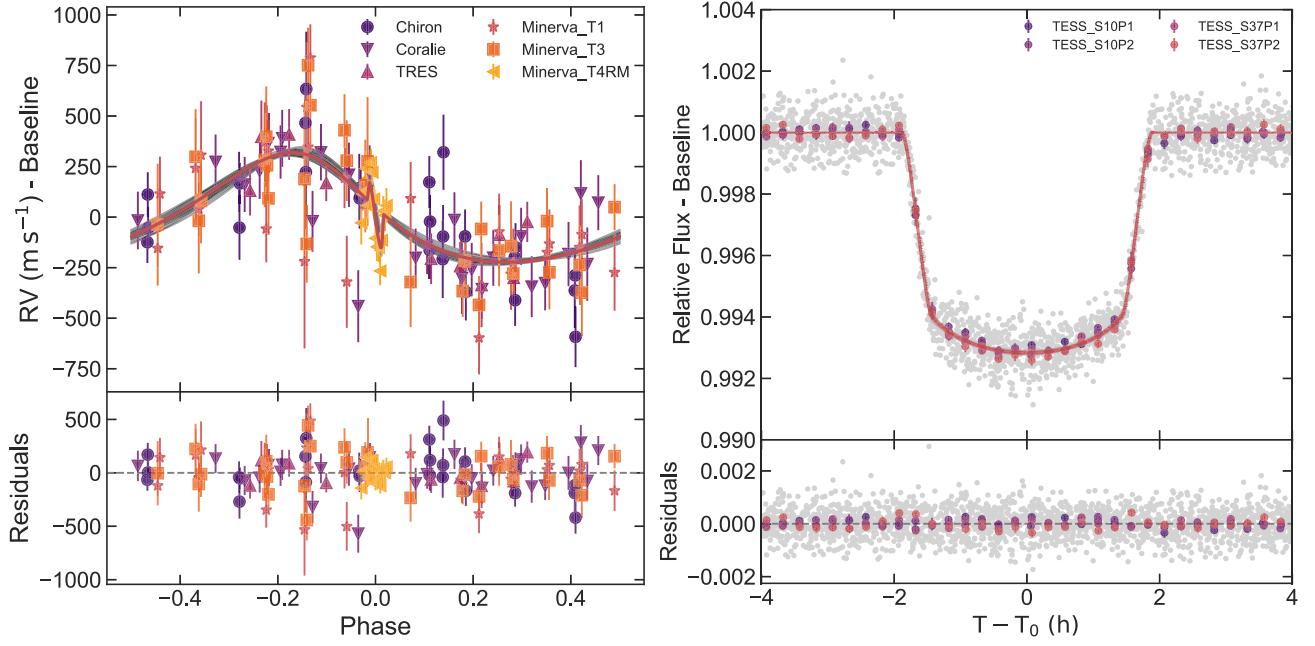


Figure 5. Left: A phase-folded radial velocity model of TOI-778 b from our *AllesFitter* analysis with the Rossiter–McLaughlin effect. Each radial velocity instrument’s data is shown, with CHIRON in violet circles, CORALIE in purple downward-pointing arrows, TRES in burgundy triangles, MINERVA-Australis Telescope 1 in pink stars, MINERVA-Australis Telescope 3 in orange squares, and MINERVA-Australis Telescope 4 in yellow leftward-pointing arrows. Twenty randomly drawn posterior radial velocity models are shown in gray lines, while the red line is the best-fit model. Residual velocities to the best-fit model are shown below. Right: Phase-folded light-curve model for TOI-778 b just from the TESS data, with the sectors (Sectors 10 and 37, respectively) and light-curve segments (P1 and P2, respectively) indicated. Phase-folded light-curve models for the ground-based follow-up are presented in Figure 6.

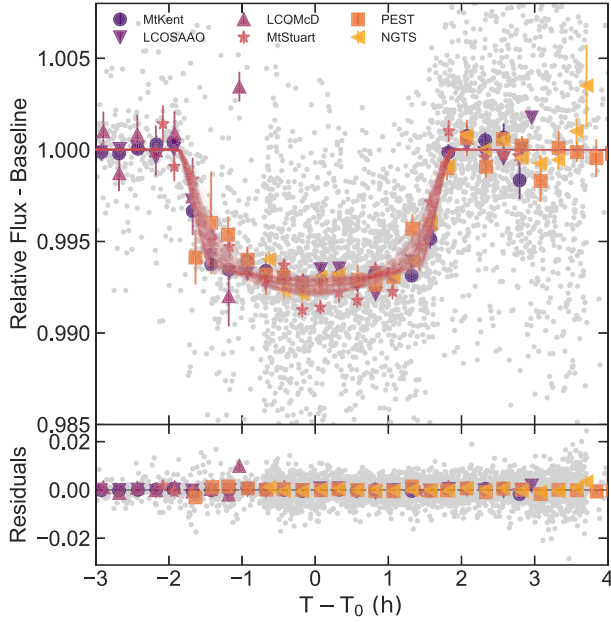


Figure 6. Phase-folded light-curve model for TOI-778 b from the ground-based observations. The colored symbols are binned observations from Mt. Kent (violet circles), LCO McDonald (burgundy up triangles), PEST (orange squares), LCO SAAO (purple downward-facing triangles), Mt. Stuart (red stars), and NGTS (yellow leftward-facing triangles). The gray points are the unbinned observations from all the ground-based facilities. One hundred randomly drawn posteriors are shown in red, with the residuals of the fits shown in bottom plot. The ground-based data behind this figure is available in machine-readable format.

(The data used to create this figure are available.)

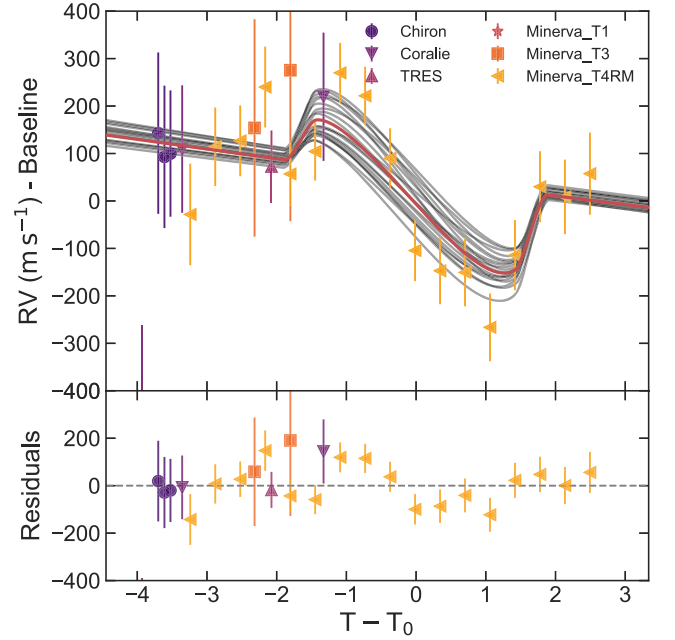


Figure 7. A phase-folded radial velocity model of the Rossiter–McLaughlin effect of TOI-778. Each radial velocity instrument’s data is shown with CHIRON in violet circles, CORALIE in purple downward-pointing arrows, TRES in burgundy triangles, MINERVA-Australis Telescope 1 in pink stars, MINERVA-Australis Telescope 3 in orange squares, and MINERVA-Australis Telescope 4 in yellow leftward-pointing arrows, similarly to Figure 5. Twenty randomly drawn posterior radial velocity models are shown as gray lines, while the best-fit model is plotted as the red line. The residuals in the velocities from the best-fit model are shown in the bottom panel.

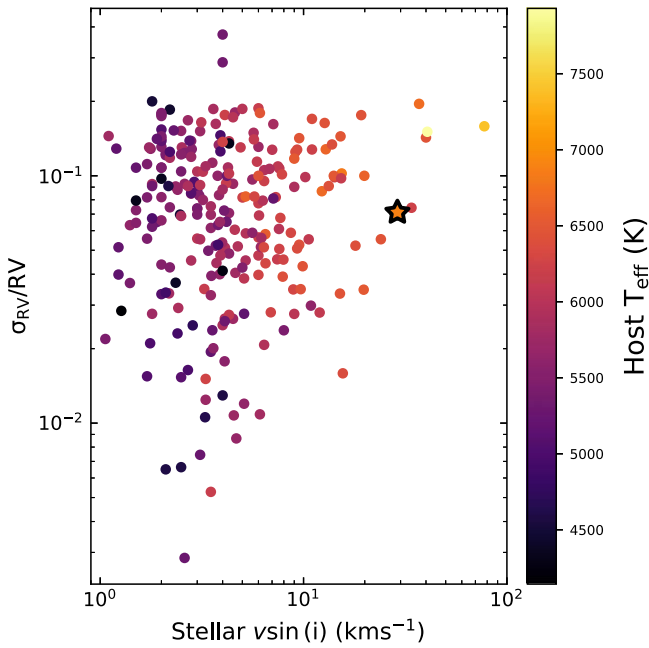


Figure 8. Host-star $v \sin i$ as a function of radial velocity amplitude precision, for 842 planets for which masses have been measured with a precision of better than 20%.

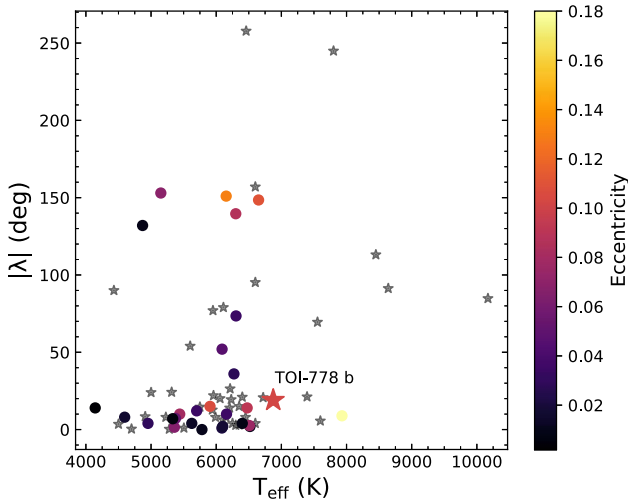


Figure 9. We show all known hot Jupiters ($R_p > 0.7 R_J$, $P_p < 10$ days) with obliquity measurements and plot those measurements against their host star's effective temperature. Points are colored by the planet's orbital eccentricity, albeit planets in circular orbits are shown as gray stars. TOI-778 b is shown as the large, red, filled-in star.

MINERVA-Australis can lead the charge of confirming and characterizing exoplanets around rapidly rotating stars.

We respectfully acknowledge the traditional custodians of all lands throughout Australia, and recognize their continued cultural and spiritual connection to the land, waterways, cosmos, and community. We pay our deepest respects to all Elders, ancestors, and descendants of the Giabal, Jarowair, and Kambuwal nations, upon whose lands the MINERVA-Australis facility at Mt Kent is situated.

MINERVA-Australis is supported by Australian Research Council LIEF Grant LE160100001, Discovery Grants

DP180100972 and DP220100365, Mount Cuba Astronomical Foundation, and institutional partners University of Southern Queensland, UNSW Sydney, MIT, Nanjing University, George Mason University, University of Louisville, University of California Riverside, University of Florida, and The University of Texas at Austin.

This paper includes data collected at the Keck Telescopes. We recognize and acknowledge the cultural role and reverence that the summit of Maunakea has within the indigenous Hawaiian community. We are deeply grateful to have the opportunity to conduct observations from this mountain.

Funding for the TESS mission is provided by NASA's Science Mission directorate. We acknowledge the use of public TESS Alert data from pipelines at the TESS Science Office and at the TESS Science Processing Operations Center. This research has made use of the Exoplanet Follow-up Observation Program website, which is operated by the California Institute of Technology, under contract with the National Aeronautics and Space Administration under the Exoplanet Exploration Program. Resources supporting this work were provided by the NASA High-End Computing (HEC) Program through the NASA Advanced Supercomputing (NAS) Division at Ames Research Center for the production of the SPOC data products. This paper includes data collected by the TESS mission, which are publicly available from the Mikulski Archive for Space Telescopes (MAST).

Some of the observations in the paper made use of the High-Resolution Imaging instrument Zorro. Zorro was funded by the NASA Exoplanet Exploration Program and built at the NASA Ames Research Center by Steve B. Howell, Nic Scott, Elliott P. Horch, and Emmett Quigley. Data were reduced using a software pipeline originally written by Elliott Horch and Mark Everett. Zorro was mounted on the Gemini South telescope of the international Gemini Observatory, a program of NSF's OIR Lab, which is managed by the Association of Universities for Research in Astronomy (AURA) under a cooperative agreement with the National Science Foundation. on behalf of the Gemini partnership: the National Science Foundation (United States), National Research Council (Canada), Agencia Nacional de Investigación y Desarrollo (Chile), Ministerio de Ciencia, Tecnología e Innovación (Argentina), Ministério da Ciência, Tecnologia, Inovações e Comunicações (Brazil), and Korea Astronomy and Space Science Institute (Republic of Korea).

We thank the Swiss National Science Foundation (SNSF) and the Geneva University for their continuous support to our planet search programs. This work has been in particular carried out in the frame of the National Centre for Competence in Research PlanetS supported by the Swiss National Science Foundation (SNSF).

This publication makes use of The Data & Analysis Center for Exoplanets (DACE), which is a facility based at the University of Geneva (CH) dedicated to extrasolar planets data visualization, exchange, and analysis. DACE is a platform of the Swiss National Centre of Competence in Research (NCCR) PlanetS, federating the Swiss expertise in Exoplanet research. The DACE platform is available at <https://dace.unige.ch>.

This work makes use of observations from the LCOGT network.

J.T.C would like to thank B.C. and D.N., and is supported by the Australian Government Research Training Program (RTP)

Scholarship. T.F. acknowledges support from the University of California President’s Postdoctoral Fellowship Program. A.J. and R.B. acknowledge support from ANID—Millennium Science Initiative—ICN12_009. A.J. acknowledges additional support from FONDECYT project 1210718. R.B. acknowledges additional support from FONDECYT Project 1120075.

All of the TESS data used in this paper can be found in MAST doi:[10.17909/t9-nmc8-f686](https://doi.org/10.17909/t9-nmc8-f686).

Facilities: Minerva-Australis, Euler1.2 m (CORALIE), LCOGT, CHIRON.

Software: *dynesty* (Speagle 2020), *ExoFAST* (Eastman 2017), *isochrones* (Morton 2015), *Allesfitter* (Günther & Daylan 2019, 2021).
























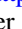
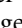
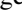









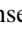






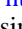
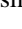
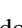
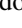








Appendix Extra Fitting Information







Table 4 in the Appendix provides extra fitting parameters used in the joint analysis of the radial velocity and transit light-curve data with *Allesfitter*, as discussed in Section 4.

Table 4
Median Values and 68% Confidence Interval of the Fitted and Derived Parameters for TOI-778

Parameter	Description	Prior	Best Fit
Radial Velocity Model Parameters			
$\ln\sigma_{\text{jitter}} (\text{RV}_{\text{Chiron}})$	RV jitter ($\ln \text{ m s}^{-1}$)	$\mathcal{U}(-3, 9)$	$1.68^{+1.58}_{-1.61}$
$\ln\sigma_{\text{jitter}} (\text{RV}_{\text{Coralie}})$	RV jitter ($\ln \text{ m s}^{-1}$)	$\mathcal{U}(-3, 9)$	$4.72^{+3.09}_{-3.14}$
$\ln\sigma_{\text{jitter}} (\text{RV}_{\text{TRES}})$	RV jitter ($\ln \text{ m s}^{-1}$)	$\mathcal{U}(-3, 9)$	$1.06^{+0.93}_{-0.97}$
$\ln\sigma_{\text{jitter}} (\text{RV}_{\text{MinervaT1}})$	RV jitter ($\ln \text{ m s}^{-1}$)	$\mathcal{U}(-3, 9)$	$1.72^{+1.66}_{-1.68}$
$\ln\sigma_{\text{jitter}} (\text{RV}_{\text{MinervaT3}})$	RV jitter ($\ln \text{ m s}^{-1}$)	$\mathcal{U}(-3, 9)$	$1.64^{+1.53}_{-1.57}$
$\ln\sigma_{\text{jitter}} (\text{RV}_{\text{MinervaT4RM}})$	RV jitter ($\ln \text{ m s}^{-1}$)	$\mathcal{U}(-3, 9)$	$1.56^{+1.44}_{-1.50}$
$\Delta\text{RV}_{\text{CHIRON}}$	RV offset (m s^{-1})	$\mathcal{U}(-1500, 1500)$	54 ± 25
$\Delta\text{RV}_{\text{CORALIE}}$	RV offset (m s^{-1})	$\mathcal{U}(-7300, -4300)$	-5788^{+26}_{-27}
$\Delta\text{RV}_{\text{TRES}}$	RV offset (m s^{-1})	$\mathcal{U}(-1300, 1600)$	206 ± 34
$\Delta\text{RV}_{\text{MinervaT1}}$	RV offset (m s^{-1})	$\mathcal{U}(-8300, -5300)$	-6722^{+33}_{-34}
$\Delta\text{RV}_{\text{MinervaT3}}$	RV offset (m s^{-1})	$\mathcal{U}(-8300, -5300)$	-6732^{+31}_{-30}
$\Delta\text{RV}_{\text{MinervaT4RM}}$	RV offset (m s^{-1})	$\mathcal{U}(-1500, 1500)$	-42 ± 29
Photometric Model Parameters			
q_1 ; TESS	Transformed limb darkening	$\mathcal{U}(0, 1)$	$0.15^{+0.04}_{-0.03}$
q_2 ; TESS	Transformed limb darkening	$\mathcal{U}(0, 1)$	$0.46^{+0.21}_{-0.18}$
q_1 ; MtKent	Transformed limb darkening	$\mathcal{U}(0, 1)$	$0.06^{+0.06}_{-0.04}$
q_2 ; MtKent	Transformed limb darkening	$\mathcal{U}(0, 1)$	$0.43^{+0.34}_{-0.28}$
q_1 ; LCO SAAO	Transformed limb darkening	$\mathcal{U}(0, 1)$	$0.16^{+0.08}_{-0.06}$
q_2 ; LCO SAAO	Transformed limb darkening	$\mathcal{U}(0, 1)$	$0.30^{+0.31}_{-0.21}$
q_1 ; LCOMcD	Transformed limb darkening	$\mathcal{U}(0, 1)$	$0.61^{+0.25}_{-0.33}$
q_2 ; LCOMcD	Transformed limb darkening	$\mathcal{U}(0, 1)$	$0.44^{+0.33}_{-0.28}$
q_1 ; MtStuart	Transformed limb darkening	$\mathcal{U}(0, 1)$	$0.84^{+0.11}_{-0.14}$
q_2 ; MtStuart	Transformed limb darkening	$\mathcal{U}(0, 1)$	$0.39^{+0.18}_{-0.17}$
q_1 ; PEST	Transformed limb darkening	$\mathcal{U}(0, 1)$	$0.35^{+0.19}_{-0.16}$
q_2 ; PEST	Transformed limb darkening	$\mathcal{U}(0, 1)$	$0.66^{+0.24}_{-0.31}$
q_1 ; NGTS	Transformed limb darkening	$\mathcal{U}(0, 1)$	$0.31^{+0.17}_{-0.12}$
q_2 ; NGTS	Transformed limb darkening	$\mathcal{U}(0, 1)$	$0.42^{+0.33}_{-0.28}$
q_1 ; MinervaT4RM	Transformed limb darkening	$\mathcal{U}(0, 1)$	$0.62^{+0.25}_{-0.30}$
q_2 ; MinervaT4RM	Transformed limb darkening	$\mathcal{U}(0, 1)$	$0.39^{+0.33}_{-0.26}$
$\ln\sigma_{\text{TESS}}$	Flux error scaling (lnrel. flux.)	$\mathcal{U}(-10, -3)$	-7.49 ± 0.01
$\ln\sigma_{\text{Mount Kent}}$	Flux error scaling (lnrel. flux.)	$\mathcal{U}(-10, -3)$	-6.39 ± 0.04
$\ln\sigma_{\text{LCO AAO}}$	Flux error scaling (lnrel. flux.)	$\mathcal{U}(-10, -3)$	-6.65 ± 0.03
$\ln\sigma_{\text{LCO McD}}$	Flux error scaling (lnrel. flux.)	$\mathcal{U}(-10, -3)$	-5.10 ± 0.03
$\ln\sigma_{\text{Mount Stuart}}$	Flux error scaling (lnrel. flux.)	$\mathcal{U}(-10, -3)$	-6.06 ± 0.03
$\ln\sigma_{\text{PEST}}$	Flux error scaling (lnrel. flux.)	$\mathcal{U}(-10, -3)$	-5.58 ± 0.03
$\ln\sigma_{\text{NGTS}}$	Flux error scaling (lnrel. flux.)	$\mathcal{U}(-10, -3)$	-5.34 ± 0.01
δ_{tr} ; TESS;S10P1	Transit depth (ppt)	Derived parameter	7.17 ± 0.04
δ_{tr} ; TESS;S10P2	Transit depth (ppt)	Derived parameter	7.17 ± 0.04
δ_{tr} ; TESS;S37P1	Transit depth (ppt)	Derived parameter	$7.17^{+0.03}_{-0.04}$
δ_{tr} ; TESS;S37P2	Transit depth (ppt)	Derived parameter	7.17 ± 0.04
δ_{tr} ; MtKent	Transit depth (ppt)	Derived parameter	7.01 ± 0.10
δ_{tr} ; LCO SAAO	Transit depth (ppt)	Derived parameter	7.16 ± 0.09
δ_{tr} ; LCOMcD	Transit depth (ppt)	Derived parameter	$7.66^{+0.29}_{-0.33}$
δ_{tr} ; MtStuart	Transit depth (ppt)	Derived parameter	$7.85^{+0.12}_{-0.11}$
δ_{tr} ; PEST	Transit depth (ppt)	Derived parameter	$7.46^{+0.20}_{-0.22}$
δ_{tr} ; NGTS	Transit depth (ppt)	Derived parameter	$7.36^{+0.16}_{-0.15}$

ORCID iDs

Jake T. Clark  <https://orcid.org/0000-0003-3964-4658>
 Brett C. Addison  <https://orcid.org/0000-0003-3216-0626>
 Jack Okumura  <https://orcid.org/0000-0002-4876-8540>
 Sydney Vach  <https://orcid.org/0000-0001-9158-9276>
 Adriana Errico  <https://orcid.org/0000-0002-0839-4257>
 Alexis Heitzmann  <https://orcid.org/0000-0002-8091-7526>
 Joseph E. Rodriguez  <https://orcid.org/0000-0001-8812-0565>
 Duncan J. Wright  <https://orcid.org/0000-0001-7294-5386>
 Mathieu Clerté  <https://orcid.org/0000-0001-8998-463X>
 Carolyn J. Brown  <https://orcid.org/0000-0001-6649-4531>
 Tara Fetherolf  <https://orcid.org/0000-0002-3551-279X>
 Robert A. Wittenmyer  <https://orcid.org/0000-0001-9957-9304>
 Peter Plavchan  <https://orcid.org/0000-0002-8864-1667>
 Stephen R. Kane  <https://orcid.org/0000-0002-7084-0529>
 Jonathan Horner  <https://orcid.org/0000-0002-1160-7970>
 John F. Kielkopf  <https://orcid.org/0000-0003-0497-2651>
 Avi Shporer  <https://orcid.org/0000-0002-1836-3120>
 C. G. Tinney  <https://orcid.org/0000-0002-7595-0970>
 Liu Hui-Gen  <https://orcid.org/0000-0001-5162-1753>
 Sarah Ballard  <https://orcid.org/0000-0002-3247-5081>
 Brendan P. Bowler  <https://orcid.org/0000-0003-2649-2288>
 Matthew W. Mengel  <https://orcid.org/0000-0002-7830-6822>
 George Zhou  <https://orcid.org/0000-0002-4891-3517>
 Avelyn David  <https://orcid.org/0000-0002-7224-5336>
 Natalie R. Hinkel  <https://orcid.org/0000-0003-0595-5132>
 Daniel Bayliss  <https://orcid.org/0000-0001-6023-1335>
 Allyson Bieryla  <https://orcid.org/0000-0001-6637-5401>
 François Bouchy  <https://orcid.org/0000-0002-7613-393X>
 Rafael Brahm  <https://orcid.org/0000-0002-9158-7315>
 Edward M. Bryant  <https://orcid.org/0000-0001-7904-4441>
 Jessie L. Christiansen  <https://orcid.org/0000-0002-8035-4778>
 David R. Ciardi  <https://orcid.org/0000-0002-5741-3047>
 Karen A. Collins  <https://orcid.org/0000-0001-6588-9574>
 Jules Dallant  <https://orcid.org/0000-0001-6763-4874>
 Allen B. Davis  <https://orcid.org/0000-0002-5070-8395>
 Matías R. Díaz  <https://orcid.org/0000-0002-2100-3257>
 Courtney D. Dressing  <https://orcid.org/0000-0001-8189-0233>
 Gilbert A. Esquerdo  <https://orcid.org/0000-0002-9789-5474>
 Jan-Vincent Harre  <https://orcid.org/0000-0001-8935-2472>
 Steve B. Howell  <https://orcid.org/0000-0002-2532-2853>
 Jon M. Jenkins  <https://orcid.org/0000-0002-4715-9460>
 Eric L. N. Jensen  <https://orcid.org/0000-0002-4625-7333>
 Andrés Jordán  <https://orcid.org/0000-0002-5389-3944>
 David W. Latham  <https://orcid.org/0000-0001-9911-7388>
 Michael B. Lund  <https://orcid.org/0000-0003-2527-1598>
 James McCormac  <https://orcid.org/0000-0003-1631-4170>
 Louise D. Nielsen  <https://orcid.org/0000-0002-5254-2499>
 Samuel N. Quinn  <https://orcid.org/0000-0002-8964-8377>
 Don J. Radford  <https://orcid.org/0000-0002-3940-2360>
 George R. Ricker  <https://orcid.org/0000-0003-2058-6662>
 Richard P. Schwarz  <https://orcid.org/0000-0001-8227-1020>
 Sara Seager  <https://orcid.org/0000-0002-6892-6948>
 Alexis M. S. Smith  <https://orcid.org/0000-0002-2386-4341>
 Chris Stockdale  <https://orcid.org/0000-0003-2163-1437>

Thiam-Guan Tan  <https://orcid.org/0000-0001-5603-6895>
 Stéphane Udry  <https://orcid.org/0000-0001-7576-6236>
 Roland Vanderspek  <https://orcid.org/0000-0001-6763-6562>
 Maximilian N. Günther  <https://orcid.org/0000-0002-3164-9086>
 Songhu Wang  <https://orcid.org/0000-0002-7846-6981>
 Joshua N. Winn  <https://orcid.org/0000-0002-4265-047X>

References

- Addison, B., Wright, D. J., Wittenmyer, R. A., et al. 2019, *PASP*, **131**, 115003
 Addison, B. C., Knudstrup, E., Wong, I., et al. 2021a, *AJ*, **162**, 292
 Addison, B. C., Tinney, C. G., Wright, D. J., et al. 2013, *ApJL*, **774**, L9
 Addison, B. C., Wang, S., Johnson, M. C., et al. 2018, *AJ*, **156**, 197
 Addison, B. C., Wright, D. J., Nicholson, B. A., et al. 2021b, *MNRAS*, **502**, 3704
 Albrecht, S., Winn, J. N., Johnson, J. A., et al. 2012, *ApJ*, **757**, 18
 Anderson, D. R., Temple, L. Y., Nielsen, L. D., et al. 2018, arXiv:1809.04897
 Baranne, A., Queloz, D., Mayor, M., et al. 1996, *A&AS*, **119**, 373
 Barbary, K. 2016, *JOSS*, **1**, 58
 Barnes, S. I., Gibson, S., Nield, K., & Cochrane, D. 2012, *Proc. SPIE*, **8446**, 844688
 Beaugé, C., & Nesvorný, D. 2012, *ApJ*, **751**, 119
 Beleznyay, M., & Kunitomo, M. 2022, *MNRAS*, **516**, 75
 Bertin, E., & Arnouts, S. 1996, *A&AS*, **117**, 393
 Blanco-Cuaresma, S. 2019, *MNRAS*, **486**, 2075
 Blanco-Cuaresma, S., Soubiran, C., Heiter, U., & Jofré, P. 2014, *A&A*, **569**, A111
 Böhm-Vitense, E. 2007, *AJ*, **133**, 1903
 Boisvert, J. H., Nelson, B. E., & Steffen, J. H. 2018, *MNRAS*, **480**, 2846
 Borucki, W. J., Koch, D., Basri, G., et al. 2010, *Sci*, **327**, 977
 Bowler, B. P., Johnson, J. A., Marcy, G. W., et al. 2010, *ApJ*, **709**, 396
 Brown, T. M., Baliber, N., Bianco, F. B., et al. 2013, *PASP*, **125**, 1031
 Bryant, E. M., Bayliss, D., McCormac, J., et al. 2020, *MNRAS*, **494**, 5872
 Buchhave, L. A., Bakos, G. Á., Hartman, J. D., et al. 2010, *ApJ*, **720**, 1118
 Butler, R. P., Marcy, G. W., Williams, E., Hauser, H., & Shirts, P. 1997, *ApJL*, **474**, L115
 Campbell, B., Walker, G. A. H., & Yang, S. 1988, *ApJ*, **331**, 902
 Cannon, A. J., & Pickering, E. C. 1993, *yCat*, **III**/135A
 Chatterjee, S., Ford, E. B., Matsumura, S., & Rasio, F. A. 2008, *ApJ*, **686**, 580
 Chontos, A., Huber, D., Latham, D. W., et al. 2019, *AJ*, **157**, 192
 Ciardi, D. R., Beichman, C. A., Horch, E. P., & Howell, S. B. 2015, *ApJ*, **805**, 16
 Claret, A., & Bloemen, S. 2011, *A&A*, **529**, A75
 Collier Cameron, A., Guenther, E., Smalley, B., et al. 2010, *MNRAS*, **407**, 507
 Collins, K. A., Kielkopf, J. F., Stassun, K. G., & Hessman, F. V. 2017, *AJ*, **153**, 77
 Cutri, R. M., Skrutskie, M. F., van Dyk, S., et al. 2003, *yCat*, **II**/246
 Davis, A. B., Wang, S., Jones, M., et al. 2020, *AJ*, **160**, 229
 Dawson, R. I., & Johnson, J. A. 2018, *ARA&A*, **56**, 175
 Dekany, R., Roberts, J., Burruss, R., et al. 2013, *ApJ*, **776**, 130
 Eastman, J. 2017, EXOFASTv2: Generalized publication-quality exoplanet modeling code, Astrophysics Source Code Library, ascl:1710.003
 Eastman, J., Gaudi, B. S., & Agol, E. 2013, *PASP*, **125**, 83
 Eastman, J. D., Rodriguez, J. E., Agol, E., et al. 2019, arXiv:1907.09480
 Fetherolf, T., Pepper, J., Simpson, E., et al. 2022, arXiv:2208.11721
 Fűrész, G. 2008, PhD thesis, Univ. Szeged, Hungary
 Furlan, E., Ciardi, D. R., Everett, M. E., et al. 2017, *AJ*, **153**, 71
 Gaia Collaboration, Brown, A. G. A., Vallenari, A., et al. 2018, *A&A*, **616**, A1
 Gaia Collaboration, Prusti, T., de Bruijne, J. H. J., et al. 2016, *A&A*, **595**, A1
 Gaidos, E., Hirano, T., Beichman, C., et al. 2022, *MNRAS*, **509**, 2969
 Gandolfi, D., Hébrard, G., Alonso, R., et al. 2010, *A&A*, **524**, A55
 Grunblatt, S. K., Huber, D., Gaidos, E., et al. 2019, *AJ*, **158**, 227
 Günther, M. N., & Daylan, T. 2019, Allesfitter: Flexible Star and Exoplanet Inference From Photometry and Radial Velocity, Astrophysics Source Code Library, ascl:1903.003
 Günther, M. N., & Daylan, T. 2021, *ApJS*, **254**, 13
 Hay, K. L., Collier-Cameron, A., Doyle, A. P., et al. 2016, *MNRAS*, **463**, 3276
 Hayward, T. L., Brandl, B., Pirger, B., et al. 2001, *PASP*, **113**, 105
 Heitzmann, A., Zhou, G., Quinn, S. N., et al. 2021, *ApJL*, **922**, L1
 Henry, G. W., Marcy, G. W., Butler, R. P., & Vogt, S. S. 2000, *ApJL*, **529**, L41
 Høg, E., Fabricius, C., Makarov, V. V., et al. 2000, *A&A*, **355**, L27
 Horner, J., Kane, S. R., Marshall, J. P., et al. 2020, *PASP*, **132**, 102001

- Houk, N., & Smith-Moore, M. 1988, Michigan Catalogue of Two-dimensional Spectral Types for the HD Stars, Vol. 4 (Ann Arbor, MI: Univ. Michigan)
- Howell, S. B., Everett, M. E., Sherry, W., Horch, E., & Ciardi, D. R. 2011, *AJ*, **142**, 19
- Ida, S., & Lin, D. N. C. 2004, *ApJ*, **616**, 567
- Ida, S., & Lin, D. N. C. 2005, *ApJ*, **626**, 1045
- Jenkins, J. M. 2002, *ApJ*, **575**, 493
- Jenkins, J. M., Chandrasekaran, H., McCauliff, S. D., et al. 2010, *Proc. SPIE*, **7740**, 77400D
- Jenkins, J. M., Tenenbaum, P., Seader, S., et al. 2020, Kepler Data Processing Handbook: Transiting Planet Search, ed. J. M. Jenkins, Kepler Science Document KSCI-19081-003
- Jenkins, J. M., Twicken, J. D., McCauliff, S., et al. 2016, *Proc. SPIE*, **9913**, 99133E
- Jensen, E. 2013, Tapir: A web interface for transit/eclipse observability, Astrophysics Source Code Library, ascl:1306.007
- Johnson, J. A., Butler, R. P., Marcy, G. W., et al. 2007, *ApJ*, **670**, 833
- Jones, M. I., Brahm, R., Wittenmyer, R. A., et al. 2017, *A&A*, **602**, A58
- Jones, M. I., Jenkins, J. S., Brahm, R., et al. 2016, *A&A*, **590**, A38
- Jordán, A., Brahm, R., Espinoza, N., et al. 2020, *AJ*, **159**, 145
- Kiefer, F. 2019, *A&A*, **632**, L9
- Kossakowski, D., Espinoza, N., Brahm, R., et al. 2019, *MNRAS*, **490**, 1094
- Kozai, Y. 1962, *AJ*, **67**, 591
- Kraft, R. P. 1967, *ApJ*, **150**, 551
- Kunimoto, M., & Matthews, J. M. 2020, *AJ*, **159**, 248
- Latham, D. W., Mazeh, T., Stefanik, R. P., Mayor, M., & Burki, G. 1989, *Natur*, **339**, 38
- Li, D., Mustill, A. J., & Davies, M. B. 2019a, *MNRAS*, **488**, 1366
- Li, J., Tenenbaum, P., Twicken, J. D., et al. 2019b, *PASP*, **131**, 024506
- Lidov, M. L. 1962, *P&SS*, **9**, 719
- Lin, D. N. C., Bodenheimer, P., & Richardson, D. C. 1996, *Natur*, **380**, 606
- Masset, F. S., & Papaloizou, J. C. B. 2003, *ApJ*, **588**, 494
- Masuda, K., & Winn, J. N. 2020, *AJ*, **159**, 81
- Mayor, M., & Queloz, D. 1995, *Natur*, **378**, 355
- McCormac, J., Pollacco, D., Skillen, I., et al. 2013, *PASP*, **125**, 548
- McCully, C., Volgenau, N. H., Harbeck, D.-R., et al. 2018, *Proc. SPIE*, **10707**, 107070K
- Morton, T. D. 2015, Isochrones: Stellar Model Grid Package, Astrophysics Source Code Library, ascl:1503.010
- Nagasawa, M., & Ida, S. 2011, *ApJ*, **742**, 72
- Nagasawa, M., Ida, S., & Bessho, T. 2008, *ApJ*, **678**, 498
- Nielsen, L. D., Bouchy, F., Turner, O., et al. 2019, *A&A*, **623**, A100
- Paredes, L. A., Henry, T. J., Quinn, S. N., et al. 2021, *AJ*, **162**, 176
- Pecaut, M. J., & Mamajek, E. E. 2013, *ApJS*, **208**, 9
- Plavchan, P., Barclay, T., Gagné, J., et al. 2020, *Natur*, **582**, 497
- Pollack, J. B., Hubickyj, O., Bodenheimer, P., et al. 1996, *Icar*, **124**, 62
- Preibisch, T., Balega, Y., Hofmann, K.-H., Weigelt, G., & Zinnecker, H. 1999, *NewA*, **4**, 531
- Queloz, D., Mayor, M., Udry, S., et al. 2001, *Msngr*, **105**, 1
- Ricker, G. R., Winn, J. N., Vanderspek, R., et al. 2015, *JATIS*, **1**, 014003
- Rodríguez Martínez, R., Gaudi, B. S., Rodríguez, J. E., et al. 2020, *AJ*, **160**, 111
- Sebastian, D., Guenther, E. W., Deleuil, M., et al. 2022, *MNRAS*, **516**, 636
- Siverd, R. J., Collins, K. A., Zhou, G., et al. 2018, *AJ*, **155**, 35
- Smith, A. M. S., Eigmüller, P., Gurumoorthy, R., et al. 2020, *AN*, **341**, 273
- Speagle, J. S. 2020, *MNRAS*, **493**, 3132
- Stassun, K. G., Oelkers, R. J., Paegert, M., et al. 2019, *AJ*, **158**, 138
- Tanaka, H., Takeuchi, T., & Ward, W. R. 2002, *ApJ*, **565**, 1257
- Temple, L. Y., Hellier, C., Anderson, D. R., et al. 2019, *MNRAS*, **490**, 2467
- Tinney, C. G., Butler, R. P., Marcy, G. W., et al. 2001, *ApJ*, **551**, 507
- Tokovinin, A., Fischer, D. A., Bonati, M., et al. 2013, *PASP*, **125**, 1336
- Trifonov, T., Kürster, M., Zechmeister, M., et al. 2017, *A&A*, **602**, L8
- Twicken, J. D., Catanzarite, J. H., Clarke, B. D., et al. 2018, *PASP*, **130**, 064502
- Virtanen, P., Gommers, R., Oliphant, T. E., et al. 2020, *NatMe*, **17**, 261
- Wang, S., Jones, M., Shporer, A., et al. 2019, *AJ*, **157**, 51
- Wheatley, P. J., West, R. G., Goad, M. R., et al. 2018, *MNRAS*, **475**, 4476
- Wittenmyer, R. A., Bergmann, C., Horner, J., Clark, J., & Kane, S. R. 2019, *MNRAS*, **484**, 4230
- Wittenmyer, R. A., Horner, J., Carter, B. D., et al. 2018, arXiv:1806.09282
- Wittenmyer, R. A., Tinney, C. G., Butler, R. P., et al. 2011, *ApJ*, **738**, 81
- Wittenmyer, R. A., Wang, S., Horner, J., et al. 2013, *ApJS*, **208**, 2
- Wittenmyer, R. A., Wang, S., Horner, J., et al. 2020, *MNRAS*, **492**, 377
- Wizinowich, P., Acton, D. S., Shelton, C., et al. 2000, *PASP*, **112**, 315
- Wright, J. T., Marcy, G. W., Howard, A. W., et al. 2012, *ApJ*, **753**, 160
- Wytenbach, A., Mollière, P., Ehrenreich, D., et al. 2020, *A&A*, **638**, A87
- Zhou, G., Bakos, G. Á., Bayliss, D., et al. 2019a, *AJ*, **157**, 31
- Zhou, G., Huang, C. X., Bakos, G. Á., et al. 2019b, *AJ*, **158**, 141
- Zhou, G., Winn, J. N., Newton, E. R., et al. 2020, *ApJL*, **892**, L21